




RESEARCH ARTICLE

Accelerated Fourier ptychographic diffraction tomography with sparse annular LED illuminations

Shun Zhou^{1,2,3,4}  | Jiayi Li^{1,2,3,4}  | Jiasong Sun^{1,2,3,4} | Ning Zhou^{1,2,3,4} | Qian Chen^{1,2} | Chao Zuo^{1,2,3,4*} 

¹School of Electronic and Optical Engineering, Nanjing University of Science and Technology, Nanjing, China

²Jiangsu Key Laboratory of Spectral Imaging & Intelligent Sense, Nanjing, China

³Smart Computational Imaging Laboratory (SCILab), Nanjing University of Science and Technology, Nanjing, China

⁴Smart Computational Imaging Research Institute (SCIRI) of Nanjing University of Science and Technology, Nanjing, China

*Correspondence

Chao Zuo, School of Electronic and Optical Engineering, Nanjing University of Science and Technology, No. 200, Xiaolingwei Street, Nanjing, Jiangsu Province 210094, China.
Email: zuochao@njjust.edu.cn

Funding information

Fundamental Research Funds for the Central Universities, Grant/Award Number: 30920032101; Leading Technology of Jiangsu Basic Research Plan, Grant/Award Number: BK20192003; National Defense Science and Technology Foundation of China, Grant/Award Number: 2019-JCJQ-JJ-381; National Natural Science Foundation of China, Grant/Award Numbers: 61905115, 62105151; Open Research Fund of Jiangsu Key Laboratory of Spectral Imaging & Intelligent Sense, Grant/Award Number: JSGP202105; Youth Foundation of Jiangsu Province, Grant/Award Numbers: BK20190445, BK20210338

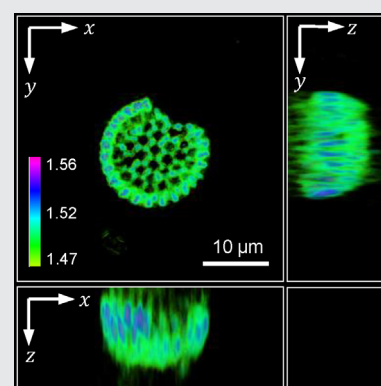
Abstract

Fourier ptychographic diffraction tomography (FPDT) is a recently developed label-free computational microscopy technique that retrieves high-resolution and large-field three-dimensional (3D) tomograms by synthesizing a set of low-resolution intensity images obtained with a low numerical aperture (NA) objective. However, in order to ensure sufficient overlap of Ewald spheres in 3D Fourier

space, conventional FPDT requires thousands of intensity measurements and consumes a significant amount of time for stable convergence of the iterative algorithm. Herein, we present accelerated Fourier ptychographic diffraction tomography (aFPDT), which combines sparse annular light-emitting diode (LED) illuminations and multiplexing illumination to significantly decrease data amount and achieve computational acceleration of 3D refractive index (RI) tomography. Compared with existing FPDT technique, the equivalent high-resolution 3D RI results are obtained using aFPDT with reducing data requirement by more than 40 times. The validity of the proposed method is experimentally demonstrated on control samples and various biological cells, including polystyrene beads, unicellular algae and clustered HeLa cells in a large field of view. With the capability of high-resolution and high-throughput 3D imaging using small amounts of data, aFPDT has the potential to further advance its widespread applications in biomedicine.

KEYWORDS

Fourier ptychographic diffraction tomography, refractive index imaging, sparse annular LED illuminations, three-dimensional imaging



Shun Zhou and Jiayi Li contributed equally to this work.

1 | INTRODUCTION

Three-dimensional (3D) refractive index (RI) contains useful quantitative biophysical information about volume, shape, size and dry mass, and these characteristics are important for morphological detection and disease diagnosis in biomedical imaging [1, 2]. As an endogenous contrast agent, 3D RI imaging of cells or tissues indeed allows the visualization of biological intracellular structure without staining or labeling. Fluorescence-based 3D imaging methods, such as confocal microscopy [3] and multiphoton microscopy [4], usually require exogenous labels (eg, fluorescent dyes or proteins) as biomarkers to provide high-contrast images of biological samples. In contrast to existing 3D fluorescence imaging, 3D RI imaging avoids the irreversible damage to living cells caused by the photobleaching and phototoxicity of fluorescent agents. Moreover, it allows high-contrast imaging to transparent biological samples which are nonfluorescent or cannot be fluorescently tagged [5–7].

Over the past two decades, quantitative phase imaging (QPI) [2] has become a widely used label-free imaging technique due to its powerful capabilities to image the phase of unstained biological samples. Some typical interferometric and noninterferometric QPI methods, including off-axis digital holograph microscopy (DHM) [8–11], common-path-based self-interference [12], transport of intensity equation [13–17], and differential phase contrast [18, 19], can provide stable QPI results for various biological cells and tissues. However, the quantitative phase only represents the total phase delay caused by nonhomogeneous RI distribution within the object, and the single two-dimensional (2D) integrated phase is insufficient for the characterization of 3D heterogeneous objects. In contrast, optical diffraction tomography (ODT) [20–25] is a powerful technique for high-resolution and high-contrast 3D label-free RI imaging. Conventional ODT is a typical tomographic technique that requires sequential measurement of multiple holograms in DHM with varying illumination angles and filling the 3D spectrum based on Fourier diffraction theorem [26, 27]. The existing interferometric setups are not compatible with commercial bright-field microscopes, and imaging quality is disturbed by the speckle noise and parasitic interference of laser sources. Furthermore, the additional intermediate phase unwrapping is required for holographic phase retrieval, which increases the complexity of the 3D RI reconstruction process.

Alternatively, intensity diffraction tomography (IDT) [28–33] does not require complicated interferometric setups and highly coherent illumination sources. Instead, only a traditional bright-field microscope with a light-emitting diode (LED) array is invoked to achieve 3D RI

imaging. The 3D RI distribution of the sample is directly recovered utilizing 3D deconvolution between the through-focus intensity stack collected by axial scanning and the optical transfer function of the system, and this direct operation makes it suitable for dynamic 3D RI tomographic imaging [34–39]. Unfortunately, the inherent trade-off between imaging resolution and contrast in IDT using a partially coherent illumination source prevents the maximum possible resolution for 3D imaging. In addition, the existing forward IDT imaging models are derived under the weakly scattering assumption (first-order Born approximation), while the Rytov approximation is more suitable for the imaging of biological cells or tissues (non-weak-phase samples) and enables the 3D RI reconstruction beyond the condition of weak objects assumption as well. Existing 3D imaging modalities are significantly limited to the space-bandwidth product of the optical system due to the usage of high-magnification objectives at the expense of the imaging field-of-view (FOV) [40].

Fourier ptychographic diffraction tomography (FPDT) [41, 42] is a recently developed label-free and noninvasive 3D microscopic imaging technique inspired by Fourier ptychographic microscopy [43–46]. Within an off-the-shelf inverted microscope and a simple programmable LED array light source, 3D tomograms are retrieved by synthesizing a set of low-resolution intensity images obtained with a low numerical aperture (NA) objective under different illumination angles. FPDT enables both large FOV and high-resolution complex 3D RI tomographic reconstruction by introducing dark-field illuminations with large angles, thanks to the inherent synthetic aperture [47, 48] and phase retrieval capabilities. Nevertheless, to ensure sufficient overlap of Ewald sphere in 3D Fourier space, conventional FPDT requires thousands of intensity measurements (capturing 3001 intensity images required [42]) and consumes a significant amount of time for stable convergence of the iterative algorithm. The imaging speed is severely limited by the huge amount of data, as evidenced by long data acquisition and computation time for tomographic reconstruction. On account of the high redundancy of a large amount of captured angled intensity stack, the sparse illumination pattern can be used to greatly reduce the data amount to be measured on the basis of ensuring imaging quality, thereby accelerating the speed of tomographic imaging.

Herein, we introduce accelerated Fourier ptychographic diffraction tomography (aFPDT) with sparse annular LED illuminations for large FOV and high-resolution 3D RI imaging with faster iteration and convergence speed. By integrating the schemes of the sparse annular LED illuminations [49, 50] and multiplexing

illumination, the issue of large data redundancy of FPDT is alleviated, in which the adoption of multiplexing illumination is inspired by Reference [45]. Based on this strategy, the distributions of LED illumination are located on annuluses with illumination NAs equal 0.4, 0.57, 0.71 and 0.8. Only 73 images were captured in our experiment, where 24 of them were bright-field intensity images with illumination NA equal to objective NA. The other 49 dark-field intensity images were acquired by multiplexing four LEDs with the same illumination NA. The validity of aFPDT is experimentally demonstrated on quantitative RI measurements of micro-polystyrene beads. Experimental results on the investigation of unstained algae and clustered HeLa cells are then presented, suggesting that the aFPDT has the potential to advance its applications in biomedicine.

2 | ALGORITHM FLOWCHART OF aFPDT

We propose the aFPDT with sparse annular LED illuminations, and the detailed algorithm flowchart is illustrated in Figure 1. The process of aFPDT reconstruction algorithm contains alternating between the spatial and Fourier domain according to the following steps:

The algorithm starts with estimating the 3D RI distribution of samples utilizing IDT [33, 35] with measured 24 bright-field intensity images. The 3D scattering potential $V(\mathbf{x})$ can be further obtained according to Equation A1. After 3D Fourier transform, the resultant spectrum is used as the initial value of $\hat{V}(\mathbf{k})$, which corresponds to Step 1 in Figure 1. The initial estimation of the scattering potential information using the result calculated by IDT

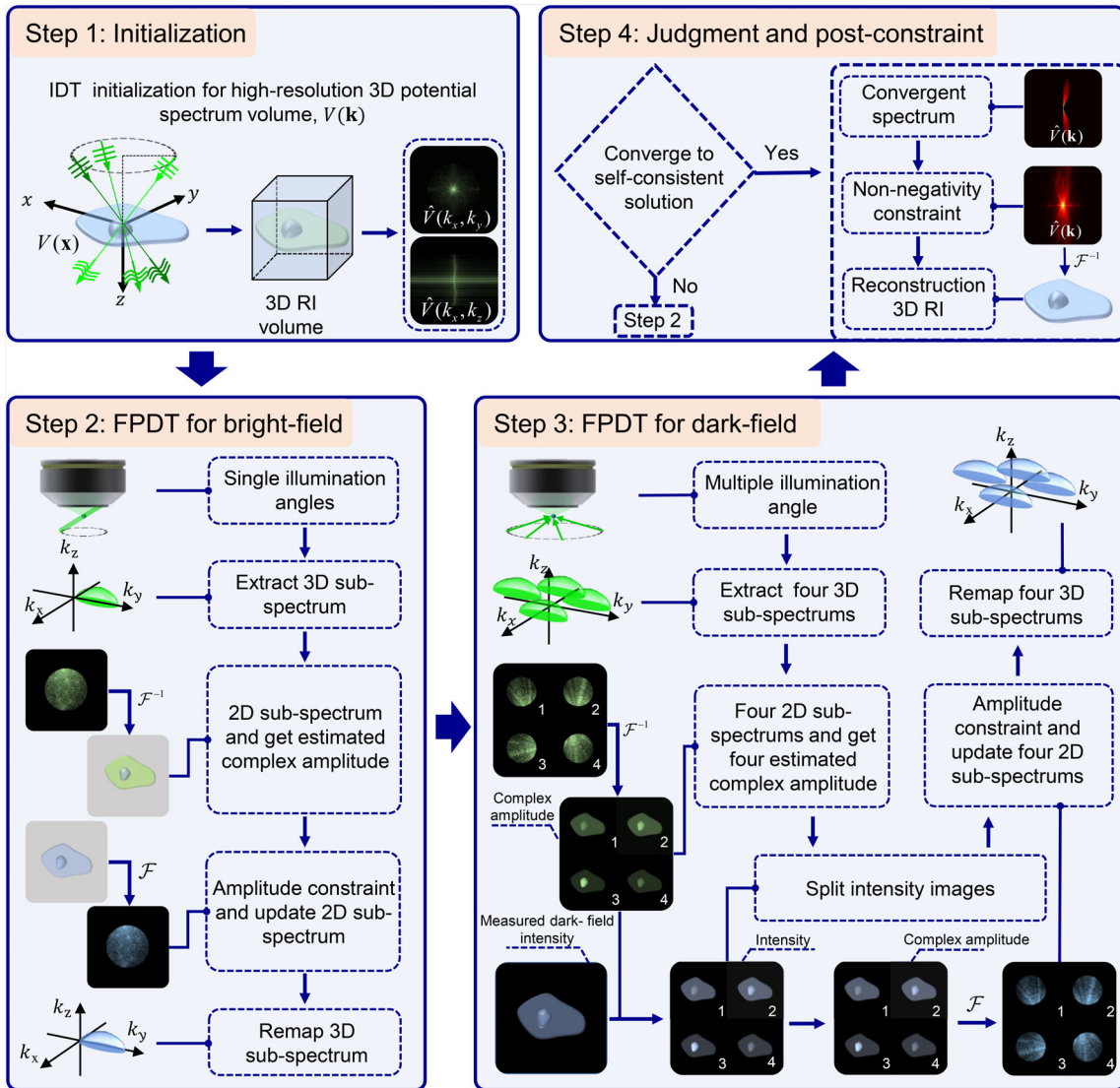


FIGURE 1 Algorithm flowchart of accelerated Fourier ptychographic diffraction tomography with sparse annular LED illuminations. 2D, Two-dimensional; 3D, three-dimensional; IDT, intensity diffraction tomography; LED, light-emitting diode; RI, refractive index

helps to avoid getting stuck in local minima under the condition of using a small amount of data.

The iterative process of aFPDT corresponds to Steps 2 and 3 in Figure 1. For the bright-field illumination of the frequency vector \mathbf{k}_i , we determine the sub-spectrum information of the corresponding support domain in the scattering potential spectrum according to the incident wave vector \mathbf{k}_i and the generalized 3D coherent transfer function, $P(\mathbf{k}_T)\delta\left(k_z - \sqrt{k_m^2 - |\mathbf{k}_T|^2}\right)$. This 3D sub-spectrum is extracted and projected along k_z direction to obtain a low-resolution 2D sub-spectrum $\hat{U}_{sl}^i(\mathbf{k}_T)$ according to

$$\hat{U}_{sl}^i(\mathbf{k}_T) = \frac{j}{4\pi k_z} \hat{V}(\mathbf{k} - \mathbf{k}_i) P(\mathbf{k}_T), \quad (1)$$

$$\delta\left(k_z - \sqrt{k_m^2 - |\mathbf{k}_T|^2}\right),$$

where the superscript i represents the i th illumination. $\hat{U}_{sl}^i(\mathbf{k}_T)$ is circular shifted in the frequency domain according to 2D incident wave vector \mathbf{k}_{iT} , and inverse Fourier transform is performed on the resultant spectrum to obtain normalized first-order scattered field $U_{sln}^i(\mathbf{x}_T)$. According to Equations A6 and A7, we convert the estimated $U_{sln}^i(\mathbf{x}_T)$ to the measured field $U_n^i(\mathbf{x}_T)$ and use the measured $I^i(\mathbf{x}_T)$ to impose an intensity constraint to obtain the updated normalized first-order scattered field $\bar{U}_{sln}^i(\mathbf{x}_T)$. The update formula is

$$\bar{U}_{sln}^i(\mathbf{x}_T) = \ln \left\{ \sqrt{I^i(\mathbf{x}_T)} \frac{\exp[U_{sln}^i(\mathbf{x}_T)]}{|\exp[U_{sln}^i(\mathbf{x}_T)]|} \right\}. \quad (2)$$

Fourier transform of this updated complex amplitude $\bar{U}_{sln}^i(\mathbf{x}_T)$ to the Fourier domain. The resultant spectrum is further shifted back to its original position, which forms the first-order scattered field after intensity constrain. According to the relation in Equation A3, the updated 2D spectrum information is remapped to the 3D cap of Ewald sphere of scattering potential spectrum for 3D spectrum coverage of bright-field illumination.

Due to the multiplexed illumination scheme, the dark-field intensity is contributed by the illumination from different angles, and it will be decomposed for the constraint and update of four different sub-spectrums in the reconstruction process. The detailed process is shown in Step 3 of Figure 1. For a certain dark-field intensity image captured under the simultaneous illumination of four known LEDs, we extract the corresponding four 3D sub-spectrums bounded by the 3D-generalized aperture from $\hat{V}(\mathbf{k})$ according to the illumination angles,

respectively. By projecting along the axial frequency coordinate, correcting constants and normalizing, we obtain four 2D normalized first-order scattered fields $U_{sln}^{i,m}(\mathbf{x}_T)$, where $m = 1, 2, 3, 4$. Next, convert the estimated $U_{sln}^{i,m}(\mathbf{x}_T)$ to normalized total field $U_n^{i,m}(\mathbf{x}_T)$. It is worth mentioning that the detailed steps are consistent with the bright-field process. As the measured intensity conforms to the principle of incoherent superposition, (ie, the intensity of four LEDs lit simultaneously is equal to the summation of the intensity of each LED lit individually), we decompose the intensity state mixture by feat of the amplitude component of $U_n^{i,m}(\mathbf{x}_T)$. The formula can be expressed as:

$$I^{i,m}(\mathbf{x}_T) = \frac{|U_n^{i,m}(\mathbf{x}_T)|^2}{\sum_{m=1}^4 |U_n^{i,m}(\mathbf{x}_T)|^2} I^i(\mathbf{x}_T). \quad (3)$$

After that, the decomposed intensity images $I^{i,m}(\mathbf{x}_T)$ are used as the intensity constraint condition to update the normalized first-order scattered field, $\bar{U}_{sln}^{i,m}(\mathbf{x}_T)$. The update formula is derived as:

$$\bar{U}_{sln}^{i,m}(\mathbf{x}_T) = \ln \left\{ \sqrt{I^{i,m}(\mathbf{x}_T)} \frac{\exp[U_{sln}^{i,m}(\mathbf{x}_T)] - 1}{|\exp[U_{sln}^{i,m}(\mathbf{x}_T)] - 1|} + 1 \right\}. \quad (4)$$

After inverse normalization and spectrum remapping, four sub-spectrums' information can be updated at once with only one dark-field intensity image, which speeds up the coverage and update of the scattering potential spectrum.

We implement iterative constraints between Steps 2 and 3 until the iterations of aFPDT converge within all intensity images (24 bright-field images and 49 dark-field images). Finally, a nonnegative iterative constraint algorithm based on prior knowledge about samples is adopted to solve the missing cone problem caused by the finite illumination angle and the limitation of the objective NA [51]. The algorithm effectively fills the spectrum information of the missing cone, which increases the RI value and eliminates axial artifacts. 3D inverse Fourier transforming the scattering potential spectrum results in the reconstruction of the 3D RI distribution of the sample to be measured [26, 27].

3 | SIMULATIONS FOR VARIOUS ILLUMINATION SCHEMES

3.1 | Various sparse illumination schemes comparison for bright-field

We implement the simulation of 3D RI reconstruction based on a pure phase microsphere with different sparse

sampling schemes of LED illumination within bright-field NA, and the simulation results are shown in Figure 2. The ideal microsphere with an 8 μm diameter and RI of 1.595 is immersed in the matched medium ($n_m = 1.58$). First, as the reference result, the 3D RI distribution of the microsphere is reconstructed utilizing complete bright-field intensity images without down-sampling the illumination angle. While for the situation of sparse illumination down-sampling, the distance between two adjacent LEDs is increased to two and four times of the original LED pixel pitch resulting in the uniform down-sample of illumination angles by two and four times, respectively [52]. The FPDT algorithm is employed to recover the 3D RI of the microsphere under the $2\times$ and $4\times$ illumination angles down-sampling, respectively. Additionally, the annular illumination matched with the NA of objective [49] is also compared with other uniform illumination down-sampling schemes, and

the reconstruction result is also shown in Figure 2. From the presented results, the sparse annular illumination scheme provides the best 3D RI reconstruction quality of the microsphere among three different illumination down-sampling schemes. The matched annular illumination (ie, $\text{NA}_{\text{ill}} = \text{NA}_{\text{obj}}$) not only eliminates the overlap of two antisymmetric circular regions in the phase transfer function, ensuring optimal low-frequency phase information coverage, but also ensures maximizing the Fourier coverage allowed by the system within the bright-field. Together, annular illumination scheme captures both high- and low-spatial frequency phase and absorption information, which is beneficial to 3D RI reconstruction using a small number of intensity-only measurements. Based on this group of simulations, the sparse annular illumination scheme is determined to reduce the amount of intensity images without seriously degrading imaging performance for bright-field situation.

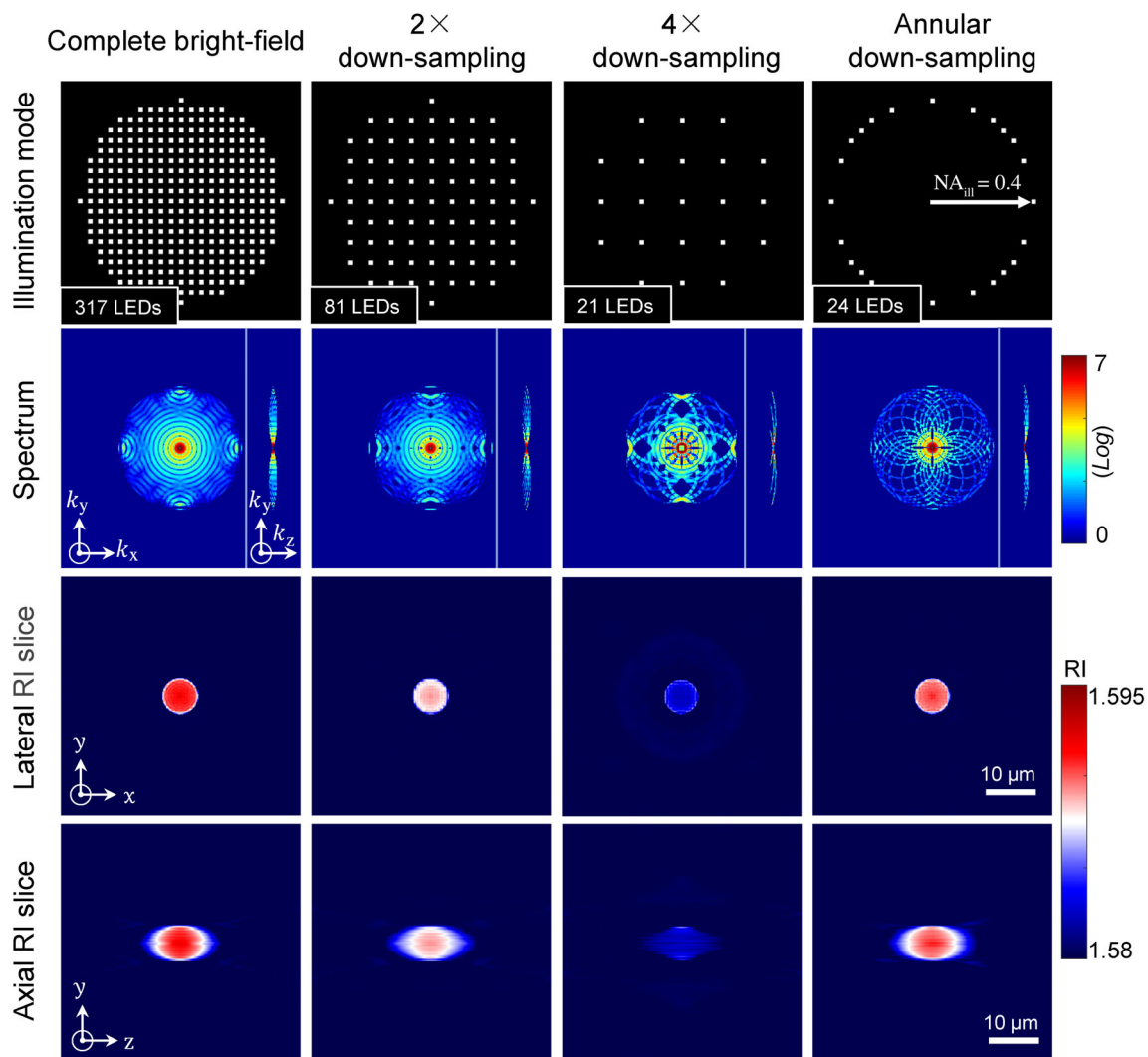


FIGURE 2 Comparison of the simulated microsphere results using FPDT algorithm under various sparse illumination schemes for bright-field. FPDT, Fourier ptychographic diffraction tomography; LED, light-emitting diode; RI, refractive index

3.2 | Various sparse illumination schemes comparison for dark-field

Based on the sparse annular illumination scheme within bright-field, the down-sampling schemes of dark-field illumination need to be considered as well to further reduce the amount of dark-field intensity data. The 3D RI reconstruction simulations for various dark-field sparse illumination schemes are performed on two microspheres and three bars, and the detailed results are shown in Figure 3.

Figures 3A,B illustrate the 3D simulation results of using only the annular bright-field illumination (24

bright-field images) and using all 2708 intensity images (2684 dark-field and 24 bright-field images), respectively. It can be seen from the microspheres edges and bars that the dark-field images are crucial for improving the resolution and recovering the details of objects. In addition, the reconstructed results with the $4\times$ down-sampling and annular down-sampling of dark-field LED illumination are presented in Figures 3C,D, respectively. There are three annular patterns for the dark-field illumination in Figure 3D, and we choose the LEDs with $NA_{\text{ill}} = 0.57$, $NA_{\text{ill}} = 0.71$ and $NA_{\text{ill}} = 0.8$. The selection of this illumination method is based on two points: First, the annular illuminations can cover the 3D scattering potential

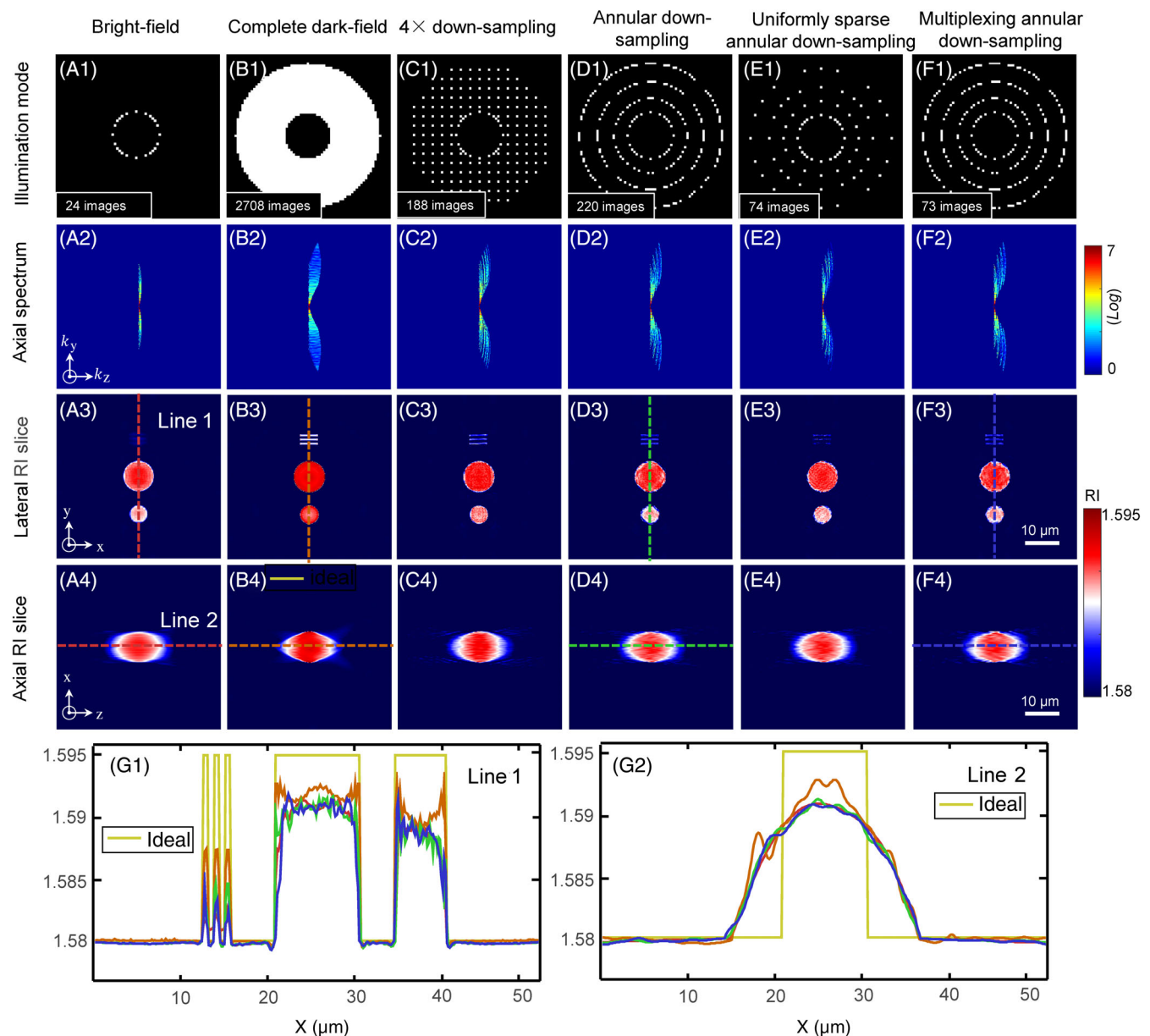


FIGURE 3 Comparison of simulated results using various dark-field illumination schemes in the case of the bright-field illumination of sparse annular pattern. RI, Refractive index

spectrum information as much as possible, accompanied by achieving theoretical lateral resolution of 421 nm and axial resolution of 1.25 μm . Second, the elaborate design of NA equal to 0.57, 0.71 and 0.8 intends to ensure the overlap of Ewald spheres with the spectrum on the adjacent inner and outer illumination NA, which enhances the constraint between the spectrum information and ensures stable convergence of the iterative algorithm. The results show that the illumination scheme of annular down-sampling for dark-field can recover the RI distribution of objects well.

Further, we perform a uniform sparse down-sampling simulation on the basis of annular dark-field illuminations (Figure 3E). However, in this case, the high-frequency details cannot be recovered properly since the amount of data is too small and the scattering potential cannot converge well. Alternatively, the combination of multiplexing strategy on the basis of annular dark-field illuminations can further reduce the intensity data requirement for dark-field manifold as well. The measured intensity under illumination multiplexing conforms to the principle of incoherent superposition. In order to ensure the uniform distribution

of superimposed intensity and avoid the signal being overwhelmed by noise, we carry out illumination angles multiplexing of the LEDs with the same illumination NA. Figure 3F shows the simulation result of four LEDs multiplexing based on the sparse annular dark-field illuminations indicating the slight quality degeneration of 3D RI reconstruction of microspheres and bars. Figures 3G1,G2 denote the lateral and axial RI line profiles corresponding to the dashed lines labeled in Figures 3A3-F4. Compared with other types of dark-field illumination, the illumination strategy corresponding to Figure 3F significantly reduces the amount of dark-field intensity data at the expense of solely slight loss of image quality. In fact, this slight loss of image quality is reasonable because the multiplexing annular illumination strategy reduces the amount of data, the spectrum coverage, and overlap of the scattering potential compared to the illumination strategy using all dark-field images.

By combining with the above bright-field and dark-field illumination scheme analysis, we finally propose an aFPDT adopting optimized sparse annular LED illuminations and multiplexing illumination scheme to achieve

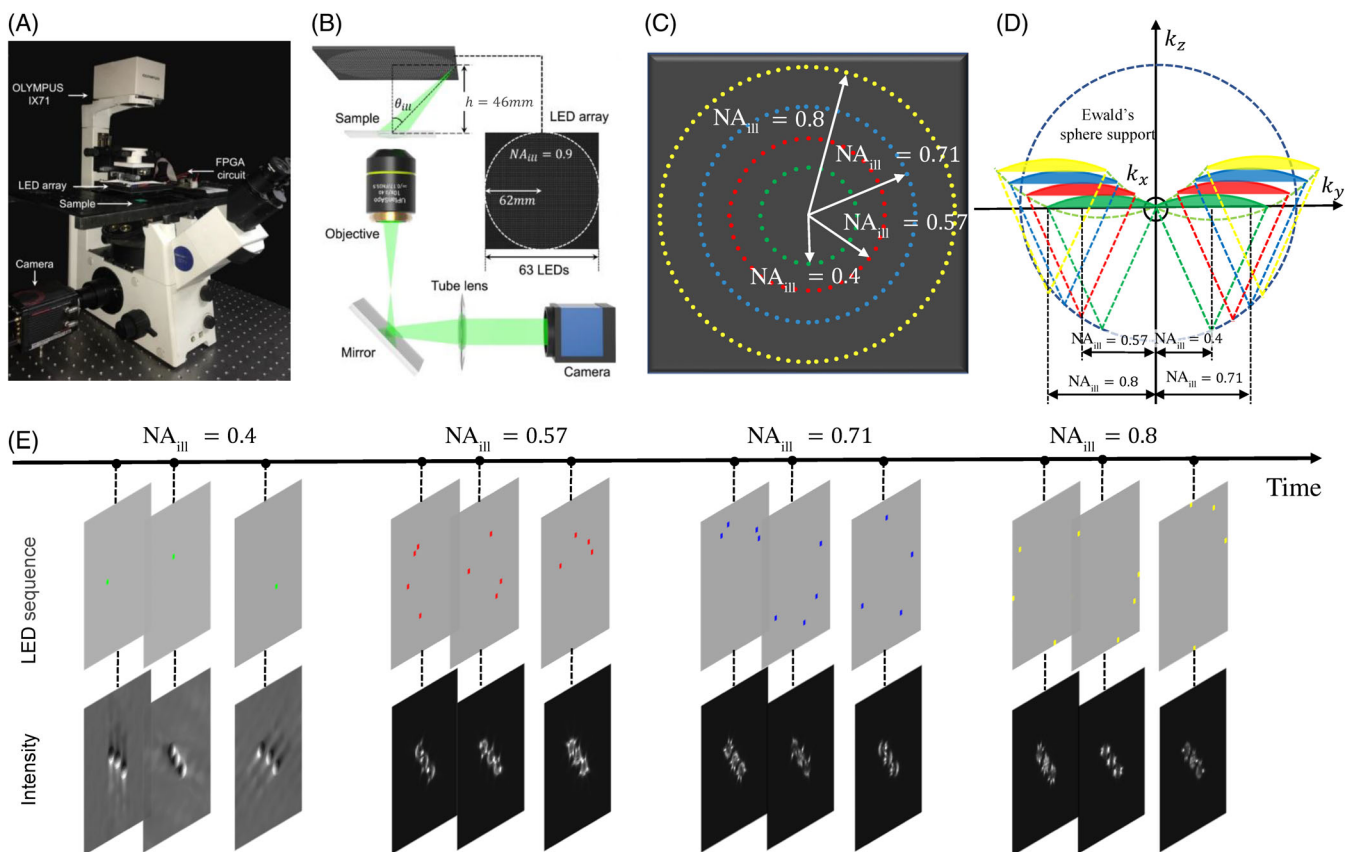


FIGURE 4 A, Photograph of the aFPDT experimental setup. B, Schematic of the aFPDT illumination imaging system. C, Description of LEDs position and illumination NA. D, 2D spectral supports in the $k_y - k_z$ plane for different illumination NA. E, Illustration of the illumination pattern and data acquisition, corresponding to the different illumination conditions in (C). aFPDT, Accelerated Fourier Ptychographic Diffraction Tomography; LED, light-emitting diode

large FOV and high-resolution 3D RI imaging with a small amount of data.

4 | EXPERIMENTAL SETUP AND IMPLEMENTATION OF aFPDT

The aFPDT is implemented on an off-the-shelf inverted bright-field microscope platform (IX71, Olympus, Japan) with a $10\times$ 0.4NA objective (UPLSAPO $10\times$, Olympus, Japan), as shown in Figure 4A. We use a programmable 63×63 LED array to replace the light source, providing quasi-coherent illumination with a center wavelength of 507 nm and spectral bandwidth of 20 nm. As depicted in Figures 4B,C, the distance between the sample stage and the LED array is 46 mm. Lateral distance between adjacent LEDs is 2 mm, and the available maximum illumination NA is 0.8. The LED array is driven by a field-programmable gate array (FPGA) unit (EP4CE10E22C8N, ALTERA), and the 24 LEDs on the LED array with illumination NAs equal to 0.4 are

individually lit one by one. For dark-field illumination, we control the FPGA to turn on four LEDs with the same illumination NA each time, which are located on an annulus on the LED array. This same operation is implemented for LEDs with illumination NA equal to 0.57, 0.71 and 0.8, respectively. Finally, a CMOS camera (Hamamatsu ORCA-Flash 4.0 C13440) with a resolution of 2048×2048 and a pixel size of $6.5\ \mu\text{m}$ is used to record the intensity information, which is synchronized with the LED array by the same controller via two coaxial cables that provide the trigger and monitor the exposure status. Under the camera exposure rate of 33 Hz, a total of 73 full-frame (2048×2048) 16-bit images are captured within 2.22 seconds, as shown in Figure 4E.

All the experimental data are processed by MATLAB software (MATLAB R2018a) with a computer workstation (Intel Core i7-7820X central processing unit operating at 3.6 GHz with 8 cores and 16 threads, 128 GB of 2133 MHz DDR4 random-access memory, NVIDIA GeForce RTX 2080Ti 11 GB graphics card). The time required for all computation processes (including 30 aFPDT iterations and

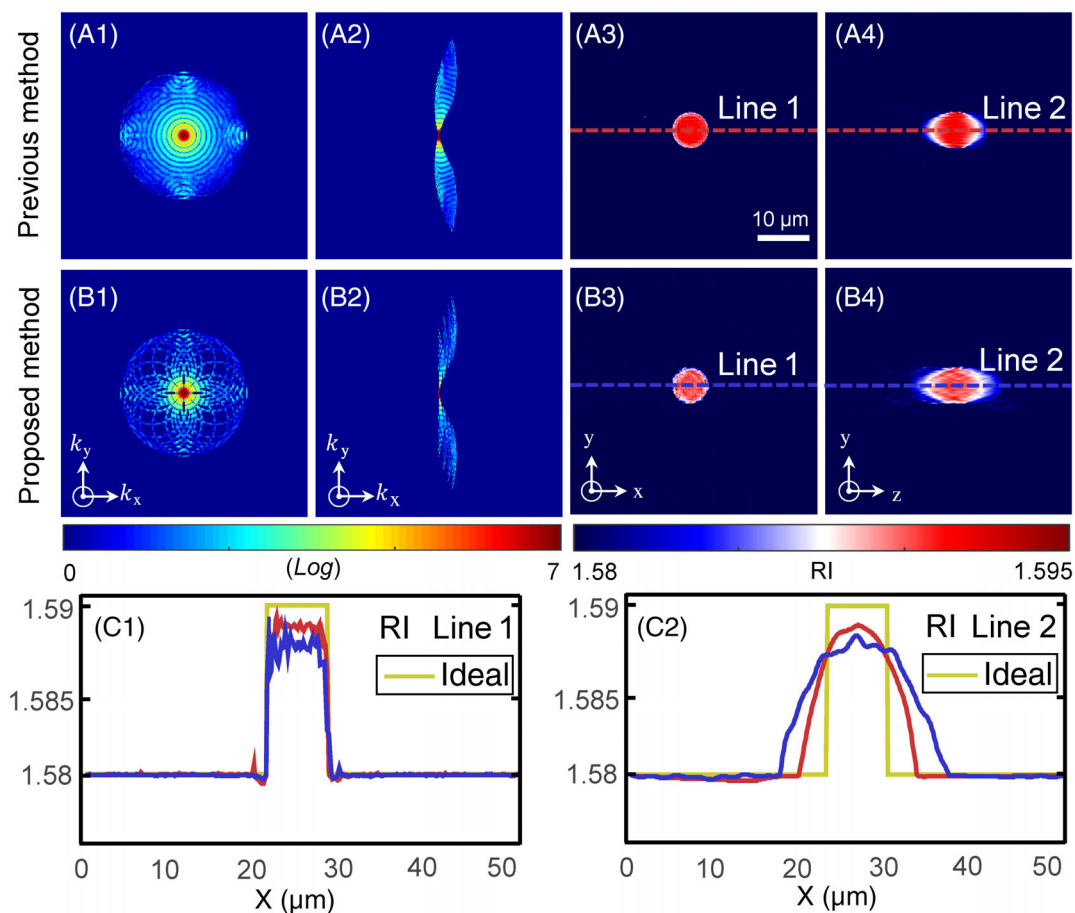
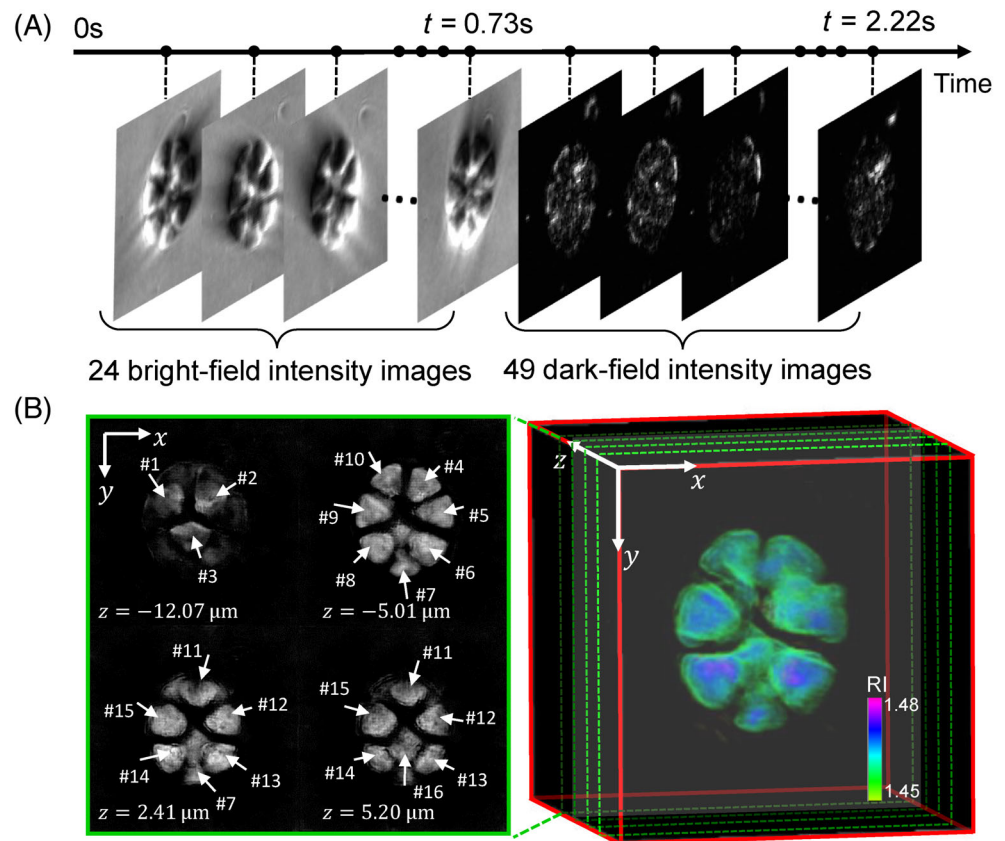


FIGURE 5 3D quantitative RI reconstruction of a micro-polystyrene bead. A1-A4, Lateral and axial spectrum and RI slices recovered using previous FPDT. B1-B4, Lateral and axial spectrum and RI slices recovered using aFPDT. C1-C2, The RI line profiles corresponding to the red and blue dashed lines labeled in A and B. aFPDT, Accelerated Fourier ptychographic diffraction tomography; RI, refractive index

FIGURE 6 3D RI tomographic imaging of unstained *Pandorina morum*. A, Time sequence of captured intensity images. B, 3D rendering of reconstructed RI and the 2D RI slices at different axial depths (see also Video S1). 2D, Two-dimensional; 3D, three-dimensional; RI, refractive index



20 iterations of the nonnegativity constraint) of intensity stacks within a small segment ($80 \times 80 \times 73$) from the whole FOV ($2048 \times 2048 \times 73$) is 21 seconds. After obtaining the high-resolution tomogram ($320 \times 320 \times 320$) of each subregion, a full FOV high-resolution 3D tomographic result ($8192 \times 8192 \times 320$) is created.

5 | EXPERIMENTAL RESULTS

5.1 | 3D RI reconstruction of a standard micro-polystyrene bead

In order to verify the applicability of the aFPDT experimentally, a micro-polystyrene bead with known RI is used for 3D tomographic imaging. The micro-polystyrene bead (Polysciences, $n = 1.59$) with an $8 \mu\text{m}$ diameter is immersed in oil (Cargille, $n_m = 1.58$). For reference, 3001 intensity images were used to recover RI distribution of the bead (Figures 5A1-A4). Figures 5B1-B4 display the reconstruction results of the same sample using the proposed method. As marked with red and blue dashed lines in Figures 5A,B, the lateral and axial profiles of bead illustrate the RI reconstruction differences between the previous method and proposed one, where the yellow lines represent the ideal values (Figures 5C1,C2). By quantitatively comparing the imaging quality, the aFPDT

can effectively recover the 3D RI distribution of samples with a small amount of data. Although there is a slight loss in imaging quality, the advantage is that the amount of data is reduced by more than 40 times, from 3001 to 73, thereby reducing images acquisition and calculation time significantly.

5.2 | 3D RI tomographic imaging of unstained *Pandorina morum*

The unstained *P. morum* is used for 3D RI measurement to test the performance of aFPDT in its intended biomedical applications. As shown in Figure 6A, 73 intensity images of the sample under different illumination angles were captured in 2.22 seconds. The right side of Figure 6B is a 3D rendering of the reconstructed RI of *P. morum*, while four RI slices at different depths are presented on the left panel. The recovered through-slice RI stacks as well as the corresponding 3D rendered images are animated in Video S1. From the result, we can intuitively see that the *P. morum* is composed of 16 cells, which are held together to form a sack globular colony surrounded by mucilage. Moreover, these cells are located at different axial depths and their intracellular RI presents differential distribution. The experimental result of *P. morum* shows that aFPDT is suitable for unlabeled biological cell imaging.

5.3 | Quantitative 3D RI measurement of diatom

We perform 3D tomographic imaging on unstained centric diatoms, which are microorganisms with transparent cell walls (called frustule) formed by the hydration of a small amount of water and silica. The frustule is composed of upper and lower valves (also known as epitheca and hypotheca). Each valve is made up of extremely complex hexagonal micropores of silica, which is arranged to form a silk network [53]. The damaged central diatom observed here is just the upper valve of the cell wall. Figure 7A shows the rendering results of the reconstructed 3D RI projected in the x-y, x-z and y-z directions. Besides, the 3D rendered images are animated in Video S2. It can be seen that the epitheca is a semi-shell shape, and the valve presents a radial silk mesh structure, which is formed by arranged hexagonal micropores composed of silica. The upper valve is surrounded by a ring of its own special processes. The original

intensity image taken under vertical illumination is illustrated in Figure 7B. Figures 7C,D1,D2 are the RI slices of the centric diatom at $z = 0 \mu\text{m}$, $z = 6.24 \mu\text{m}$ and $z = 8.97 \mu\text{m}$. In addition, as marked with the blue and red lines in Figures 7D1,D2, the RI line profiles shown in Figures 7E1,E2 allow us to obtain the quantitative biological information of process and silica microporous skeleton: (1) The spacing between two adjacent processes is between $2\sim 3 \mu\text{m}$, and the diameter of the hexagonal micropores is about $3 \mu\text{m}$, and (2) the RI of process is higher than that of the reticulated silica skeleton.

5.4 | Full FOV tomographic imaging of unstained HeLa cells

In the last part of the experimental results, aFPDT is applied to perform 3D tomographic imaging of clustered HeLa cells to demonstrate its effective performance for

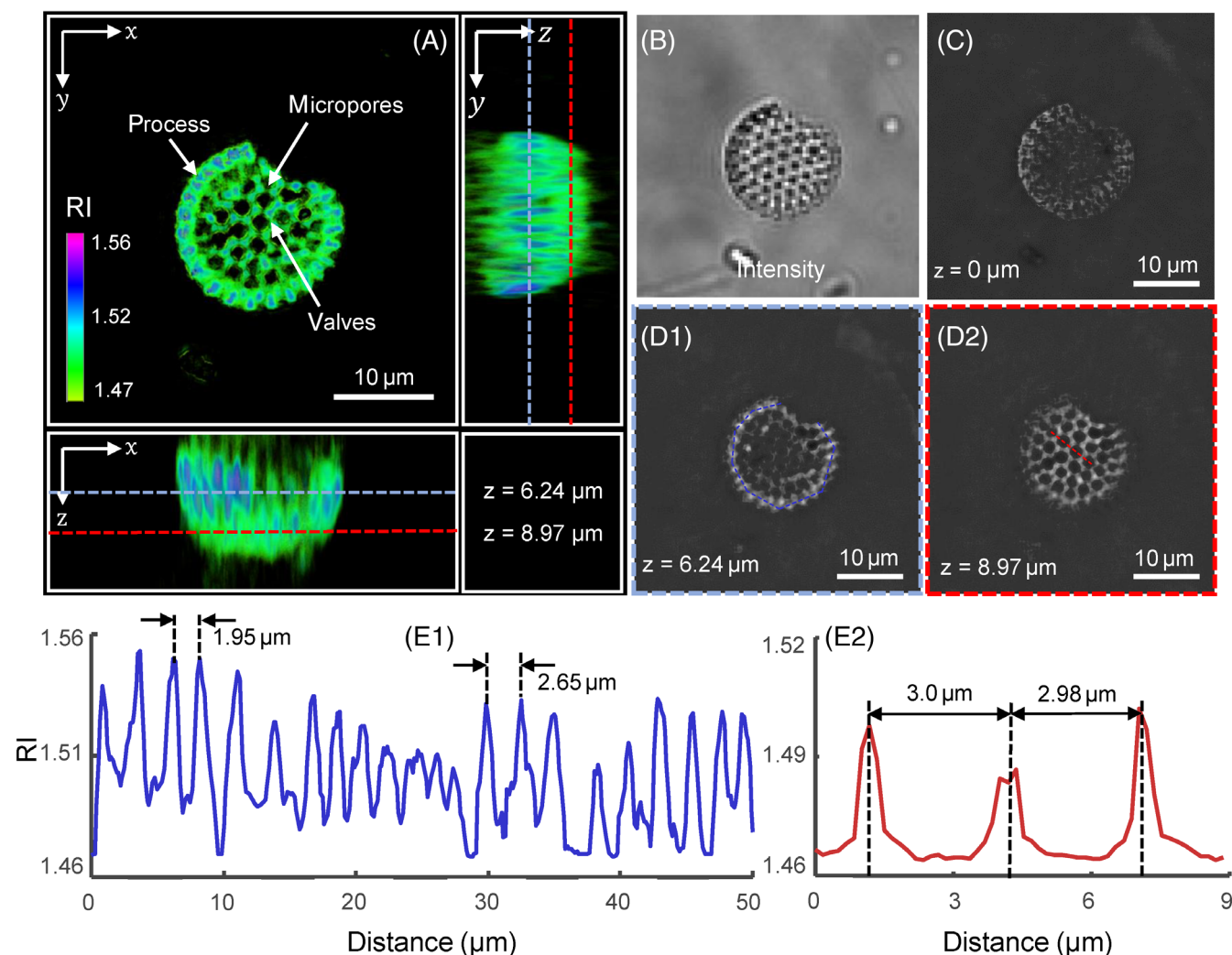
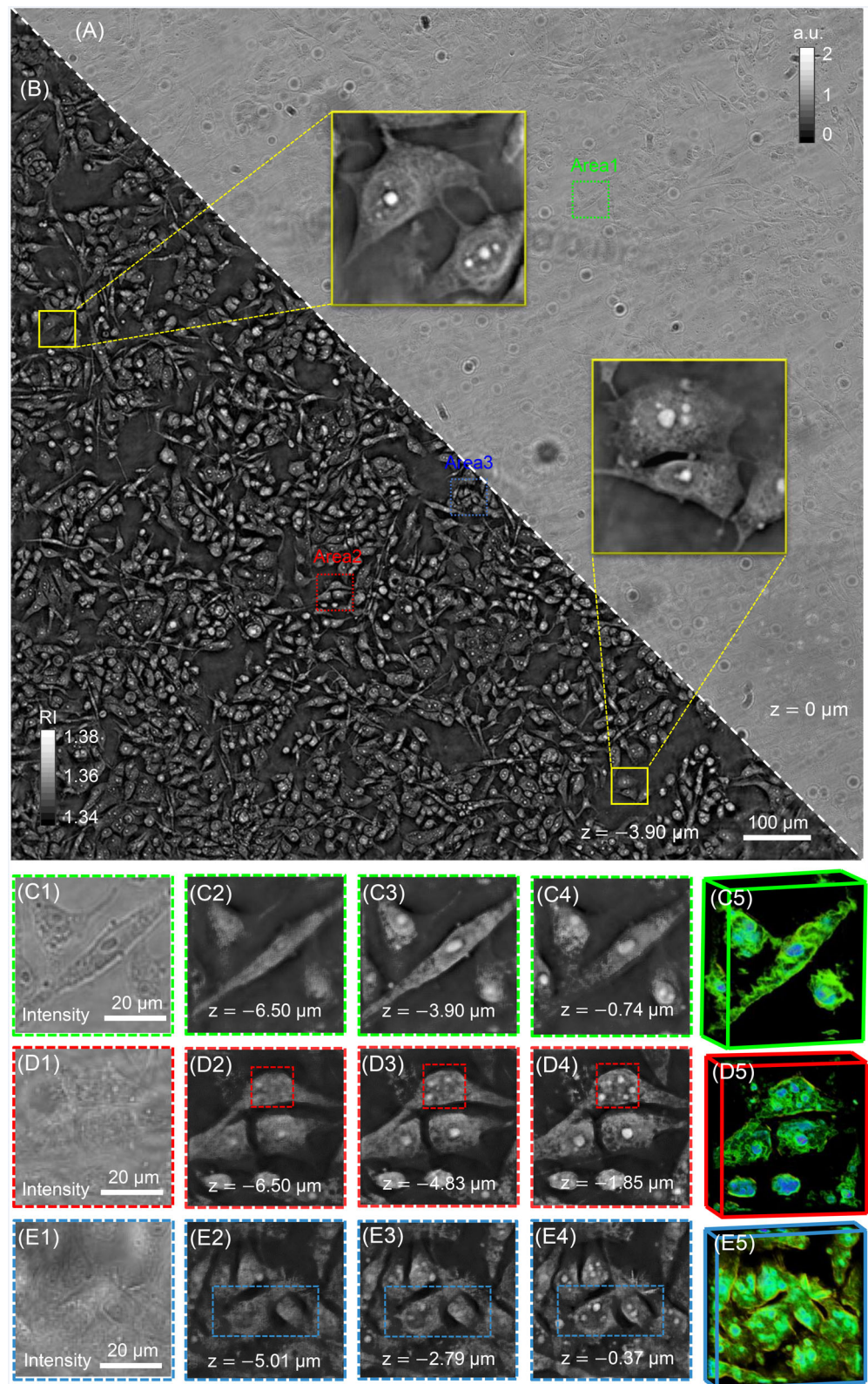


FIGURE 7 Quantitative 3D RI reconstruction of a diatom. A, Rendered x-y, x-z and y-z RI projections for diatom. B, Intensity image of diatom collected at vertical illumination. C, D1-D2, RI slices of diatom at $z = 0 \mu\text{m}$, $z = 6.24 \mu\text{m}$ and $z = 8.97 \mu\text{m}$. E1-E2, RI line profiles corresponding to the blue line in D1 and red line in D2 (see also Video S2). 3D, Three-dimensional; RI, refractive index

FIGURE 8 Full FOV high-resolution 3D RI imaging of HeLa cells. A, Full FOV intensity image of HeLa cells collected under a 10 \times objective at vertical illumination. B, The full FOV RI slice of HeLa cells at $z = -3.90 \mu\text{m}$ was reconstructed using aFPDT. C1-E1, Three amplified intensity images corresponding to Area 1, Area 2, and Area 3. C2-E4, RI slices of three subregions at multiple axial depths in the results of reconstructed full FOV RI. C5-E5, 3D RI rendering results of three subregions (see also Video S3) 3D, Three-dimensional; FOV, field of view; RI, refractive index



large FOV imaging. The HeLa cells used in the experiment are immersed in phosphate-buffered saline buffer with RI of 1.34. Figure 8A displays a full FOV intensity image of HeLa cells taken under a 10 \times objective at vertical illumination, with a FOV of 1.77 mm², which

exhibits very weak imaging contrast due to the weak absorption of the cells. The full FOV RI slice of HeLa cells reconstructed at $z = -3.9 \mu\text{m}$ using aFPDT is illustrated in Figure 8B. In order to clearly illustrate the sub-cellular structure of HeLa cells, three subregions

(52 μm \times 52 μm) in Figures 8A,B are amplified. Figures 8C1-E1 is the amplified intensity images corresponding to Area 1, Area 2 and Area 3, respectively. The reconstruction results of RI slices corresponding to the three subregions at multiple axial depths are shown in Figures 8C2-E4. From the results, we can clearly see the 3D subcellular structure with high contrast including nucleus and cytoskeletal fibers. Due to the excellent axial sectioning capability, 3D tomographic imaging provides more detailed subcellular features in different axial slices instead of 2D phase information, and we can well determine the 3D distribution of organelles throughout the entire volume as well as quantify the RI of organelles. Further, the rendering results of 3D RI reconstruction for three different subregions present the 3D morphology and internal structure of cells (Figures 8C5-E5). The final recovered full FOV RI, stacks along the axial direction, and 3D rendering results are also provided in Video S3 for better visualization.

6 | CONCLUSION AND DISCUSSION

We introduced aFPDT, a high-resolution and high-throughput tomographic imaging technique for 3D evaluation of unstained specimens. By effectively merging the schemes of the optimized sparse annular LED illuminations and multiplexing illumination, only 73 intensity images under different illumination angles were measured and synthesized in Fourier domain to recover sample's 3D RI distribution. Herein, the simulations and analysis of various schemes for bright-field and dark-field illumination have demonstrated that the hybrid strategy of sparse annular and multiplexing illuminations is effective. With the proposed illumination strategy, we have reduced the system's data requirement more than 40 times from 3001 to 73, which not only relieves the burden on both storage and processing but also achieves computational acceleration of 3D tomographic reconstruction. In addition, we exhibited the detailed algorithm process and experimental setup platform to describe how we use aFPDT to achieve 3D RI tomographic imaging. The technique has also been experimentally verified on 3D RI measurement of a micro-polystyrene bead. Experimental results for investigation of unstained algae and HeLa cells are then presented, suggesting the high efficiency of aFPDT for large FOV and high-resolution 3D RI tomographic imaging using a small amount of data. We believe this method has the potential to advance its widespread applications in biomedicine, providing noninvasive 3D tomographic imaging of unlabeled weak scattering specimens.

Moreover, aFPDT is expected to be further optimized. From the perspective of improving the experimental setup, by properly redesigning the LED illuminator [54, 55] to guarantee a uniform overlap for the high- and low-frequency region of the 3D object spectrum, the reconstruction is expected to be successful with much fewer intensity measurements. Furthermore, polychromatic capture raw data set has not been attempted, which can potentially provide more additional information about volumetric samples for the same amount of data [56]. In addition, rapid update algorithms of the spectrum will be our following work to explore the fast convergence of the iterative process. Finally, our reconstruction approach based on aFPDT is constrained by unknown experimental variables, including position misalignment and coherence of LED illumination. These variables are difficult to be fully parameterized via an analytical model but may be overcome using emerging learning-based direct inversion techniques [57–61]. By merging these approaches, it is possible to realize high-fidelity 3D RI tomographic imaging and increase the construction speed from 21 seconds per 3D frame to less than 10 seconds per 3D frame for a subregion, enabling the extended application of aFPDT in the field of high-quality dynamic monitoring of cell morphology and dynamics in the future.

CONFLICT OF INTEREST

The authors declare no conflicts of interest.

DATA AVAILABILITY STATEMENT

The data that support the findings of this study are available from the corresponding author upon reasonable request.

ORCID

Shun Zhou  <https://orcid.org/0000-0002-7033-1513>

Jiaji Li  <https://orcid.org/0000-0001-6206-7700>

Chao Zuo  <https://orcid.org/0000-0002-1461-0032>

REFERENCES

- [1] Y. K. Park, C. Depeursinge, G. Popescu, *Nat Photonics* **2018**, *12*, 578.
- [2] G. Popescu, *Quantitative Phase Imaging of Cells and Tissues*, McGraw-Hill Education, New York **2011**.
- [3] R. H. Webb, *Rep. Prog. Phys.* **1996**, *59*, 427.
- [4] A. Diaspro, *Confocal and Two-Photon Microscopy*, Wiley-Liss, New York **2002**.
- [5] D. J. Stephens, V. J. Allan, *Science* **2003**, *300*, 82.
- [6] S. Waldchen, J. Lehmann, T. Klein, S. Van De Linde, M. Sauer, *Sci. Rep.* **2015**, *5*(1), 1.
- [7] Y. Fan, J. Li, L. Lu, J. Sun, Y. Hu, J. Zhang, Z. Li, Q. Shen, B. Wang, R. Zhang, Q. Chen, C. Zuo, *Photonix* **2021**, *2*, 19.
- [8] B. Kemper, G. Von Bally, *Appl. Optics* **2008**, *47*, A52.
- [9] P. Ferraro, D. Alferi, S. De Nicola, L. De Petrocellis, A. Finizio, G. Pierattini, *Opt. Lett.* **2006**, *31*, 1405.

- [10] F. Merola, P. Memmolo, L. Miccio, R. Savoia, M. Mugnano, A. Fontana, G. D'ippolito, A. Sardo, A. Iolascon, A. Gambale, P. Ferraro, *Light: Sci. Appl.* **2017**, 6, e16241.
- [11] R. Zhao, L. Huang, Y. Wang, *PhotonIX* **2020**, 1(1), 1.
- [12] Z. Wang, L. Millet, M. Mir, H. Ding, S. Unarunotai, J. Rogers, *Opt. Express* **2011**, 19, 1016.
- [13] L. Waller, L. Tian, G. Barbastathis, *Opt. Express* **2010**, 18, 12552.
- [14] C. Zuo, J. Sun, J. Li, J. Zhang, A. Asundi, Q. Chen, *Sci. Rep.* **2017**, 7(1), 1.
- [15] J. Li, Q. Chen, J. Zhang, Y. Zhang, L. Linpeng, C. Zuo, *Biomed. Opt. Express* **2017**, 8, 4687.
- [16] Y. Bao, T. K. Gaylord, *JOSA A* **2016**, 33, 2125.
- [17] C. Zuo, J. Li, J. Sun, Y. Fan, J. Zhang, L. Linpeng, R. Zhang, B. Wang, L. Huang, Q. Chen, *Opt. Lasers Eng.* **2020**, 135, 106187.
- [18] L. Tian, L. Waller, *Opt. Express* **2015**, 23, 11394.
- [19] Y. Fan, J. Sun, Q. Chen, X. Pan, L. Tian, C. Zuo, *Photonics Res.* **2019**, 7, 890.
- [20] A. C. Kak, M. Slaney, *Principles of computerized tomographic imaging*, SIAM, Philadelphia, Pennsylvania **2001**.
- [21] W. Choi, C. Fang-Yen, K. Badizadegan, O. Seungeun, N. Lue, R. R. Dasari, M. S. Feld, *Nat. Methods* **2007**, 4, 717.
- [22] Y. Sung, W. Choi, C. Fang-Yen, K. Badizadegan, R. R. Dasari, M. S. Feld, *Opt. Express* **2009**, 17, 266.
- [23] Y. Cotte, F. Toy, P. Jourdain, N. Pavillon, D. Boss, P. Magistretti, P. Marquet, C. Depeursinge, *Nat Photonics* **2013**, 7, 113.
- [24] S. Shin, K. Kim, J. Yoon, Y. K. Park, *Opt. Lett.* **2015**, 40, 5407.
- [25] A. Kuś, W. Krauze, and M. Kujawińska. *Three-Dimensional and Multidimensional Microscopy: Image Acquisition and Processing XXII*. International Society for Optics and Photonics: San Francisco, CA, **2015**.
- [26] E. Wolf, *Opt. Commun.* **1969**, 1, 153.
- [27] V. Lauer, *J. Microsc.* **2002**, 205, 165.
- [28] N. Streibl, *JOSA A* **1985**, 2, 121.
- [29] M. Chen, L. Tian, L. Waller, *Biomed. Opt. Express* **2016**, 7, 3940.
- [30] J. M. Soto, J. A. Rodrigo, T. Alieva, *Opt. Express* **2017**, 25, 15699.
- [31] J. Li, Q. Chen, J. Sun, J. Zhang, J. Ding, C. Zuo, *Biomed. Opt. Express* **2018**, 9, 2526.
- [32] J. Huang, Y. Bao, T. K. Gaylord, *JOSA A* **2020**, 37, 1857.
- [33] R. Ling, W. Tahir, H.-Y. Lin, H. Lee, L. Tian, *Biomed. Opt. Express* **2018**, 9, 2130.
- [34] J. A. Rodrigo, J. M. Soto, T. Alieva, *Biomed. Opt. Express* **2017**, 8, 5507.
- [35] J. Li, A. C. Matlock, Y. Li, Q. Chen, C. Zuo, L. Tian, *Adv. Photonics* **2019**, 1, 066004.
- [36] A. Matlock, L. Tian, *Biomed. Opt. Express* **2019**, 10, 6432.
- [37] J. Li, A. Matlock, Y. Li, Q. Chen, L. Tian, C. Zuo, *Photonics Res.* **2020**, 8, 1818.
- [38] T. Nguyen, M. Kandell, G. Popescu, *Conf. on Lasers and Electro-optics: Science and Innovations*, Optical Society of America, San Jose, CA, **2016**.
- [39] D. Dong, X. Huang, L. Li, H. Mao, Y. Mo, G. Zhang, Z. Zhang, J. Shen, W. Liu, Z. Wu, G. Liu, Y. Liu, H. Yang, Q. Gong, K. Shi, L. Chen, *Light: Sci. Appl.* **2020**, 9(1), 1.
- [40] A. W. Lohmann, R. G. Dorsch, D. Mendlovic, Z. Zalevsky, C. Ferreira, *JOSA A* **1996**, 13, 470.
- [41] R. Horstmeyer, J. Chung, O. Xiaozhe, G. Zheng, C. Yang, *Optica* **2016**, 3, 827.
- [42] C. Zuo, J. Sun, J. Li, A. Asundi, Q. Chen, *Opt. Lasers Eng.* **2020**, 128, 106003.
- [43] G. Zheng, R. Horstmeyer, C. Yang, *Nat Photonics* **2013**, 7, 739.
- [44] O. Xiaozhe, R. Horstmeyer, C. Yang, G. Zheng, *Opt. Lett.* **2013**, 38, 4845.
- [45] L. Tian, X. Li, K. Ramchandran, L. Waller, *Biomed. Opt. Express* **2014**, 5, 2376.
- [46] C. Zuo, J. Sun, Q. Chen, *Opt. Express* **2016**, 24, 20724.
- [47] Y. Sung, A. Tzur, O. Seungeun, W. Choi, V. Li, R. R. Dasari, Z. Yaqoob, M. W. Kirschner, *PNAS* **2013**, 110, 16687.
- [48] Z. Cheng, D. Jin, Y. He, H. Lin, J. Hu, Z. Yaqoob, *Adv. Photonics* **2020**, 2, 065002.
- [49] K. Kim, *Opt. Express* **2013**, 21(26), 32269.
- [50] J. Li, N. Zhou, Z. Bai, S. Zhou, Q. Chen, C. Zuo, *Opt. Lasers Eng.* **2021**, 143, 106624.
- [51] D. Dong, K. Shi, *Adv. Photonics* **2020**, 2, 020501.
- [52] J. Sun, Q. Chen, Y. Zhang, C. Zuo, *Opt. Express* **2016**, 24, 15765.
- [53] G. A. Fryxell, G. R. Hasle, *Am. J. Bot.* **1980**, 67, 804.
- [54] J. Sun, C. Zuo, L. Zhang, Q. Chen, *Sci. Rep.* **2017**, 7, 1.
- [55] K. Guo, S. Dong, P. Nanda, G. Zheng, *Opt. Express* **2015**, 23, 6171.
- [56] T. Kim, R. Zhou, M. Mir, S. D. Babacan, P. S. Carney, L. L. Goddard, G. Popescu, *Nat Photonics* **2014**, 8, 256.
- [57] S. Jiang, K. Guo, J. Liao, G. Zheng, *Biomed. Opt. Express* **2018**, 9, 3306.
- [58] Y. Rivenson, Y. Zhang, *Light: Sci. Appl.* **2018**, 7, 17141.
- [59] G. Barbastathis, A. Ozcan, G. Situ, *Optica* **2019**, 6, 921.
- [60] Y. Xue, S. Cheng, Y. Li, L. Tian, *Optica* **2019**, 6, 618.
- [61] S. Feng, Q. Chen, G. Guohua, T. Tao, L. Zhang, H. Yan, W. Yin, C. Zuo, *Adv. Photonics* **2019**, 1, 025001.
- [62] P. M. Morse, H. Feshbach, *Am. J. Phys.* **1954**, 22, 410.
- [63] C. W. McCutchen, *JOSA* **1964**, 54, 240.

SUPPORTING INFORMATION

Additional supporting information may be found in the online version of the article at the publisher's website.

How to cite this article: S. Zhou, J. Li, J. Sun, N. Zhou, Q. Chen, C. Zuo, *J. Biophotonics* **2021**, e202100272. <https://doi.org/10.1002/jbio.202100272>

APPENDIX

A. Forward Model of FPDT

The principle of FPDT is to solve the wave equation through intensity-only constraint iteration, and the 3D RI distribution of the sample can be retrieved from multiple intensity images obtained under various illumination angles. The RI information of thick biological sample is encoded in the optical scattering potential [26] defined by the function:

$$V(\mathbf{x}) = k_0^2 [n^2(\mathbf{x}) - n_m^2], \quad (\text{A1})$$

where $\mathbf{x} = (\mathbf{x}_T, z) = (x, y, z)$. $k_0 = 2\pi/\lambda_0$ is the wave number with λ_0 being the illumination wavelength in

free space, while $n(\mathbf{x})$ and n_m are the RI of specimen and its surrounding medium, correspondingly.

While a thin sample is illuminated by a plane wave, the total transmitted field is the product of the incident field and the sample's 2D complex amplitude. Different from 2D imaging of thin samples, for the case of thick samples under a plane wave illumination $U_{in}(\mathbf{x})$, the resulting total field $U(\mathbf{x})$ is the superposition of the incident field $U_{in}(\mathbf{x})$ and the scattered field $U_s(\mathbf{x})$ (ie, $U(\mathbf{x}) = U_{in}(\mathbf{x}) + U_s(\mathbf{x})$). To obtain the analytical solution to the inverse scattering problem, the FPDT is derived based on the Rytov approximation [22], which considers the single scattering events excluding multiple scattering. It is worth mentioning that the Rytov approximation is used here to derive the linear relationship between the measured intensity and the scattering potential rather than the Born approximation since the Rytov approximation is more suitable for imaging biological cells or tissues. The first-order scattered field $U_{s1}(\mathbf{x})$ under Rytov approximation is defined as

$$\begin{aligned} U_{s1}(\mathbf{x}) &\approx U_{in}(\mathbf{x}) \ln \left[\frac{U(\mathbf{x})}{U_{in}(\mathbf{x})} \right], \\ &= U_{in}(\mathbf{x}) \ln \left[\frac{U_s(\mathbf{x}) + U_{in}(\mathbf{x})}{U_{in}(\mathbf{x})} \right]. \end{aligned} \quad (A2)$$

Further, by employing Green's function [62], the linearized relation between the scattering potential of the sample and the first-order scattered field in Fourier space can be expressed as:

$$\begin{aligned} \hat{V}(\mathbf{k} - \mathbf{k}_i) &= -4\pi j k_z \hat{U}_{s1}(\mathbf{k}_T) P(\mathbf{k}_T) \\ &\delta \left(k_z - \sqrt{k_m^2 - |\mathbf{k}_T|^2} \right), \end{aligned} \quad (A3)$$

where $\mathbf{k} = (\mathbf{k}_T, k_z) = (k_x, k_y, k_z)$ represents the 3D coordinate of the spectral space and $\mathbf{k}_i = (\mathbf{k}_{iT}, k_{iz}) = (k_{ix}, k_{iy}, k_{iz})$ is the 3D incident plane wave vector. While j is the imaginary unit and k_m is the wave number in the medium. $\hat{V}(\mathbf{k})$ and $\hat{U}_{s1}(\mathbf{k}_T)$ correspond to the 3D and 2D Fourier transforms of $V(\mathbf{x})$ and $U_{s1}(\mathbf{x}_T)$, respectively. $P(\mathbf{k}_T)$ ideally is circ-function and $P(\mathbf{k}_T) \delta \left(k_z - \sqrt{k_m^2 - |\mathbf{k}_T|^2} \right)$ is defined as 3D coherent transfer function [63], whose spectrum support domain is a restricted Ewald sphere limited by the objective aperture. Equation A3 describes the Fourier diffraction theory, in which a 2D Fourier spectrum of first-order scattered field is mapped onto the surface of an Ewald sphere according to the incident wave vector \mathbf{k}_i for a certain illumination angle.

Considering that intensity-only images are utilized to realize RI tomographic imaging, we should establish the relationships between measured intensity images and the scattering potential of samples. The measured intensity images under bright-field and dark-field can be written as:

$$\begin{aligned} I(\mathbf{x}_T) &= |U(\mathbf{x}_T)|^2, \\ &= \begin{cases} |U_{in}(\mathbf{x}_T) + U_s(\mathbf{x}_T)|^2 \text{BF}, \\ |U_s(\mathbf{x}_T)|^2 \text{DF}. \end{cases} \end{aligned} \quad (A4)$$

In addition, we defined three new variables $U_n(\mathbf{x}_T)$, $U_{sn}(\mathbf{x}_T)$ and $U_{s1n}(\mathbf{x}_T)$, to simplify the FPDT algorithm:

$$\begin{cases} U_n(\mathbf{x}_T) = U(\mathbf{x}_T)/U_{in}(\mathbf{x}_T), \\ U_{sn}(\mathbf{x}_T) = U_s(\mathbf{x}_T)/U_{in}(\mathbf{x}_T), \\ U_{s1n}(\mathbf{x}_T) = U_{s1}(\mathbf{x}_T)/U_{in}(\mathbf{x}_T), \end{cases} \quad (A5)$$

which represent the normalization of $U_n(\mathbf{x}_T)$, $U_{sn}(\mathbf{x}_T)$ and $U_{s1n}(\mathbf{x}_T)$ to the incident light $U_{in}(\mathbf{x}_T)$, respectively. With these new variables, Equation A2 can be rewritten as

$$U_{s1n}(\mathbf{x}_T) \approx \ln[U_n(\mathbf{x}_T)] = \ln[U_{sn}(\mathbf{x}_T) + 1]. \quad (A6)$$

Therefore, the connection between the measured field $U_n(\mathbf{x}_T)$ and the first-order scattered field $U_{s1n}(\mathbf{x}_T)$ for the Rytov approximation can be expressed as the following inverse relation

$$U_n(\mathbf{x}_T) = \begin{cases} \exp[U_{s1n}(\mathbf{x}_T)] \text{BF}, \\ \exp[U_{s1n}(\mathbf{x}_T)] - 1 \text{DF}. \end{cases} \quad (A7)$$

Without loss of generality, the incident illumination can be treated as an angled plane wave with a unit amplitude $U_{in}(\mathbf{x}_T) = \exp(j\mathbf{k}_{iT}\mathbf{x}_T)$, so the normalization process will not modify the intensities of the detected fields, and Equation A4 can be simplified as follows:

$$I(\mathbf{x}_T) = |U(\mathbf{x}_T)|^2 = |U_n(\mathbf{x}_T)|^2. \quad (A8)$$

In the course of the experiment, we will divide the intensity images containing samples' information by the background intensity to obtain normalized values so that the measured data conform to Equation A8. Substituting Equations A7 and A8 into Equation A3, the determined relationship between measured intensity and the scattering potential is established, and the forward imaging model of FPDT can be obtained as well.

B. Two Approximations to the Scattered Field

To get the analytical formula (Equation A3), under certain conditions, two approximations can be applied to find a solution. Equation A3 suggests that in the 3D spectrum space, the scattering potential frequency spectrum of the sample is the splicing of first-order scattered fields of different illumination angles. As is clear here, the solution requires the first-order scattered field $U_{s1}(\mathbf{x})$ either to be a measurable quantity or can be obtained by other means. Two approximations are often used to determine $U_{s1}(\mathbf{x})$.

When the RI values of the sample are close to its surrounding medium, the light scattering should be very weak. In this case, it can be assumed that the scattered field is negligible compared to the incident field $U_{in}(\mathbf{x}) \gg U_s(\mathbf{x})$ so that $U_{s1}(\mathbf{x}) \approx U_s(\mathbf{x})$. It should be noted that the scattering of object is assumed to be weak under first-order Born approximation. In other words, the absorption introduced by the sample is weak and the overall phase delay should be much smaller than π . In fact, the Born approximation only allows imaging of optical thin samples is a serious drawback. When the sample is large or its RI is much higher than that of the medium, the Rytov approximation, a second approach to determine $U_{s1}(\mathbf{x})$, is preferred.

The Rytov approximation assumes that the total field has a complex phase function, that is, $U(\mathbf{x}) = \exp[\phi(\mathbf{x})]$ and $U_{in}(\mathbf{x}) = \exp[\phi_{in}(\mathbf{x})]$. The complex phase of the total

field is the sum of the complex phase of the incident field and the scattered field:

$$\phi(\mathbf{x}) = \phi_{in}(\mathbf{x}) + \phi_s(\mathbf{x}). \quad (\text{A9})$$

Substituting Equation A9 into $U_s(\mathbf{x}) = U(\mathbf{x}) - U_{in}(\mathbf{x})$, the scattered field can be expressed as

$$U_s(\mathbf{x}) = U_{in}(\mathbf{x}) \{ \exp[\phi_s(\mathbf{x})] - 1 \}. \quad (\text{A10})$$

Thus, the complex phase of the scattered field can be expressed as the following inverse relation:

$$\phi_s(\mathbf{x}) = \ln \left[\frac{U_s(\mathbf{x})}{U_{in}(\mathbf{x})} + 1 \right]. \quad (\text{A11})$$

The first-order scattered field $U_{s1}(\mathbf{x})$ we need to determine is equal to the product of the incident field $U_{in}(\mathbf{x})$ and the complex phase of the scattered field $\phi_s(\mathbf{x})$ when the phase gradient introduced by the object is small, so we get the first-order scattered field expression as shown in Equation A2. The validity of Rytov approximation is not dependent on the overall phase delay introduced by the sample but on the gradient of the RI within the sample, and it has been shown to lead to a reconstruction that is superior to that of the Born approximation for imaging thick biological samples.